YALE PEABODY MUSEUM

JOURNAL OF MARINE RESEARCH

The *Journal of Marine Research,* one of the oldest journals in American marine science, published important peer-reviewed original research on a broad array of topics in physical, biological, and chemical oceanography vital to the academic oceanographic community in the long and rich tradition of the Sears Foundation for Marine Research at Yale University.

An archive of all issues from 1937 to 2021 (Volume 1–79) are available through EliScholar, a digital platform for scholarly publishing provided by Yale University Library at https://elischolar.library.yale.edu/.

Requests for permission to clear rights for use of this content should be directed to the authors, their estates, or other representatives. The *Journal of Marine Research* has no contact information beyond the affiliations listed in the published articles. We ask that you provide attribution to the *Journal of Marine Research.*

Yale University provides access to these materials for educational and research purposes only. Copyright or other proprietary rights to content contained in this document may be held by individuals or entities other than, or in addition to, Yale University. You are solely responsible for determining the ownership of the copyright, and for obtaining permission for your intended use. Yale University makes no warranty that your distribution, reproduction, or other use of these materials will not infringe the rights of third parties.

A numerical model of instabilities in the Florida Current

by Douglas B. Boudra,[1] Rainer Bleck[1] and Friedrich Schott[1,2]

ABSTRACT

An isopycnic coordinate numerical model is configured as an infinitely long channel with the width and bottom topography of the Straits of Florida at 27N to investigate the possibility that Florida Current meanders are due to dynamical instabilities. One mass/flow configuration with which to initialize the model is developed primarily from theoretical considerations, a second from the analysis of STACS observations (Leaman *et al.,* 1987). To ascertain the effect of the bottom topography, flat bottom experiments are first examined. The current is found to be baroclinically unstable in the classical sense (Eady, 1949) to perturbations with wavelengths greater than ~85 km, and the meanders which develop eventually dominate the channel flow pattern. When the 27N topography is included, the instability is greatly reduced, but the primary source of perturbation energy remains the baroclinic one. The meanders thus produced have wavelengths, periods, and amplitudes similar to those documented in the literature (Schmitz and Richardson, 1968; Lee and Mayer, 1977; Johns and Schott, 1987). The results are briefly compared with De Szoeke's (1975) application of his theory of *modified Eady* and *hybrid* instabilities to the Straits of Florida. From an energetics standpoint the instabilities in the model appear to be similar to the latter. From the point of view of wavelength, period and e-folding time of the most rapidly growing wave, however, they most resemble the topographically *modified Eady* instabilities.

1. Introduction

The portion of the Gulf Stream system extending eastward out of the Gulf of Mexico through the Straits of Florida and then northward along the east Florida shelf break is known as the Florida Current. Because of its conspicuous role in the North Atlantic Ocean circulation and the observationally convenient channel-like geometry of the Straits, this current is historically one of the best studied and its mean structure one of the most well-defined of the world ocean. Within the Straits, the Current transports an annual mean 30–32 × 10^6 m^3 s^{-1} of water northward (Niiler and Richardson, 1973; Leaman *et al.,* 1987). Superimposed on this mean flow, fluctuations with amplitude as large as 15–30% of the mean and with periods ranging from a few days to interannual are also known to exist. Johns and Schott (1987) and Schott *et al.* (1988) report that a substantial portion of the transport variance is in periods of several days to a few weeks.

1. Rosenstiel School of Marine and Atmospheric Science, University of Miami, Miami, Florida, 33149, U.S.A.
2. Present address: Institute fur Meereskunde, Universitat Kiel, Kiel, Federal Republic of Germany.

Fluctuations with these periods are explained primarily as a response to fluctuations in northward (downstream) wind stress (Lee *et al.,* 1986; Johns and Schott, 1987; Schott *et al.,* 1988; Lee and Williams, 1988).

The Florida Current is also observed to meander through the Straits (Schmitz and Richardson, 1968; Duing, 1975; Lee and Mayer, 1977; Brooks and Niiler, 1977; Johns and Schott, 1987; Zantopp *et al.,* 1987). Downstream scales of the meanders vary from 70–80 km up to a few hundred kilometers, and their periods, like those of the most energetic transport fluctuations, vary from 2–3 days to a few weeks. Cross-channel current core displacements of as much as 25 km have been observed off the Keys (Schmitz and Richardson, 1968), east of Miami/Ft. Lauderdale (Lee and Mayer, 1977), and north of the Straits (Zantopp *et al.,* 1987). It has been suggested, however, notably by Schmitz and Richardson (1968) and Johns and Schott (1987), that the meander amplitudes generally decrease downstream from the Gulf, as the channel becomes narrower, until the eastern boundary disappears at approximately 27.5N (see also Leaman and Molinari, 1987).

While the major transport fluctuations and meanders through the Straits have approximately the same range of temporal scales, Johns and Schott (1987) found no strong correlation between them. North of the Straits, however, Zantopp *et al.* (1987) found a substantial total transport variation (22×10^6 m^3 s^{-1}) in association with a strong meander (20 km current core displacement).

Detailed observations of the Florida Current were reported as early as 20 years ago by Schmitz and Richardson (1968). However, the first comprehensive observational program to focus on a particular section of the Current over an interannual period was executed in 1982–1984 as part of the Subtropical Atlantic Climate Studies Program (STACS). During this period, an array of moored current meters was positioned across the Straits at 27N where, in addition, numerous cruises were conducted using the PEGASUS current profilers, as well as XBTs and CTDs. The primary goal of the program was to identify convenient methods for monitoring the behavior of the flow through the Straits on a continuous basis. For example, induction measurements from a submarine communications cable stretched across the Straits near 27N might provide a relatively accurate record of total transport fluctuations, and so a check against the analysis of moored current meter data was desired. In addition, the STACS observations and subsequent analysis provide a wealth of new information describing the mean and fluctuating behavior of the Florida Current (Lee *et al.,* 1986; Molinari *et al.,* 1985; Larsen and Sanford, 1985; Leaman *et al.,* 1987; Leaman and Molinari, 1987; Johns and Schott, 1987; Schott *et al.,* 1988).

Of primary interest in the current paper is whether the meanders within the Straits are due to local instabilities, or are merely propagating downstream from the Gulf and decaying. Lee and Mayer (1977) have suggested that baroclinic instability is unlikely in the Straits of Florida because the ratio of the Rossby radius of deformation to the radius of the observed eddies (formed in the cyclonically curved portion of the

meanders) is substantially greater than one. They further point out that a necessary condition for barotropic instability—that the potential vorticity gradient in the direction normal to the coast change sign—is met in the cyclonic shear region near the Florida coast. In a paper demonstrating the possibility of *hybrid* and *modified Eady* baroclinic instabilities due to interaction with cross-stream bottom topographic variation, De Szoeke (1975) concluded that such instabilities are possible in the Straits. A condition for which he obtained instability was that the ratio of bottom to deep isopycnal slope, which we will refer to as δ_B, is negative, as is found eastward of the deepest part of the Straits. This configuration is special to channel-type geometry for subtropical western boundary currents—that is, for right-bounded currents looking downstream (left-bounded in the Southern Hemisphere).

Attempts to determine whether energy is, in the mean, being transferred from the mean flow to the meanders within the Straits have suggested that this is not the case, or if it is, that the mean conversion is very small. Brooks and Niiler (1977) performed an energetics analysis of one summer's data collected across 26°50′ and found no significant mean energy conversion between the mean and fluctuation components of flow. In the analysis of STACS PEGASUS data, Leaman *et al.* (1987) found the mean barotropic and baroclinic conversions to be from eddies to the mean flow, but in fact so small as to be statistically of indeterminate sign. Johns and Schott's (1987) energetics analysis of moored current meter data at 27N suggests that, in the mean, eddy kinetic energy is being converted to mean kinetic, and that the mean potential to eddy kinetic energy conversion is slightly greater than zero, but basically neutral.

Despite the lack of strong evidence that they result from local instabilities, vigorous meanders nonetheless exist in the Straits, as depicted here in Figure 1 (from Lee and Mayer, 1977) and as suggested by several flow reversals at a current meter deployed near the 27N shelf break during another recent observational program (Lee *et al.*, 1986). Further examination of this question seems warranted. Availability of the STACS observational analyses offers the special opportunity to initialize and verify a numerical model of the Florida Current with observed conditions and statistics. A model of this type may be used to determine in a more convincing fashion whether the mean analyzed current is barotropically or baroclinically unstable. In what follows, we detail the initial outcome of such a modeling endeavor. Here, we focus on the properties of the Florida Current at 27N, but the method is sufficiently general that it may be extended to investigate the stability of the Current at any specific position within the Straits or to the north. We show results using both (1) an idealized initialization procedure (first with a flat bottom and then with 27N topography) which incorporates basic parameters from the STACS analyses, and (2) a development of initial conditions based on the mean STACS PEGASUS hydrographic and flow field analyzed data (27N topography only).

In each case, the stability of the current to a broad range of perturbation wavelengths is investigated. It is shown that, within the flat bottom channel, the
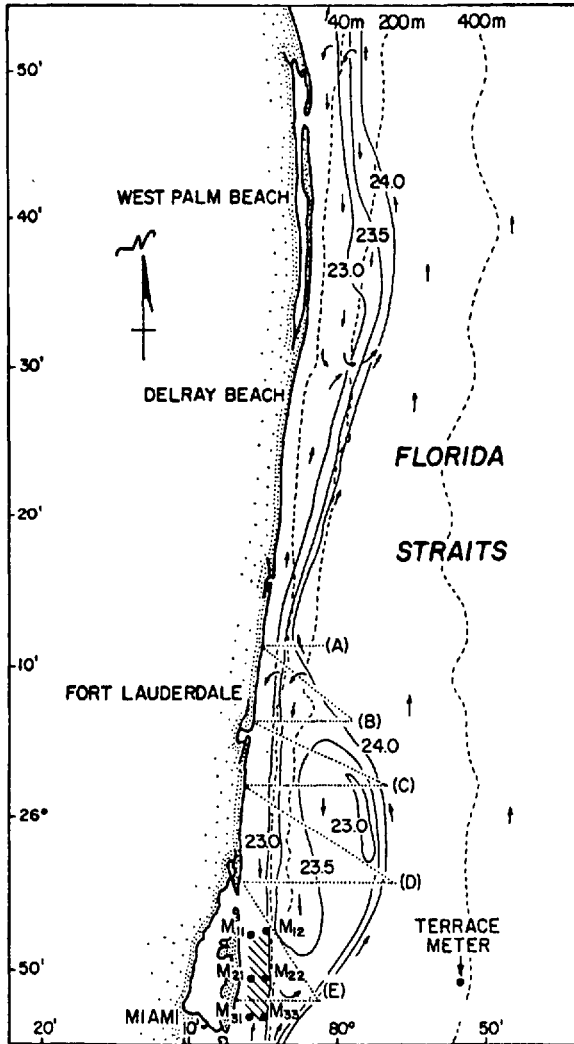
Figure 1. Composite map of surface temperature (°C) for the period 20 to 23 February, 1973. Ship track designated by dots; temperature sections by letter (A)-(E), current meter moorings by blackened circles; arrows indicate observed current direction (after Lee and Mayer, 1977).

current is baroclinically unstable to perturbations of wavelength greater than 60 km. Perturbation growth is particularly large for wavelengths in the range 150 to 210 km. When the real 27N bathymetry is introduced, the current first exhibits weak barotropic conversion, which after a few days yields to greater baroclinic conversion. It is marginally unstable, however, and this only when the cross-stream density variation is large enough—that is, when the mass/flow structure is sufficiently baroclinic.

Meanders tend to grow and decay in a series of events, as opposed to in a long period of amplification in the flat bottom case. With the analysis of STACS observations as initial conditions, the current also first exhibits weak barotropic instability, but the primary meander growth draws from the baroclinic energy source. While the meander amplitudes become larger than with the idealized data set, they are still only about half as large as obtained in the flat bottom channel. And a small amount of meander growth quickly releases the instability, leaving behind no substantial changes to the mean structure.

In both cases with the 27N bathymetry, the wavelength (λ) and period of the perturbations which reach maximum amplitude in individual λ experiments are approximately the same as those of the 170 km wavelength/5 day period meander extracted by Johns and Schott (1987) from the STACS current meter mooring data. This mode is the shortest of two dominant ones found in their analysis. In addition, the maximum amplitudes of these meanders are consistent with those observed. X–Z cross-sections of perturbation energy are compared with those analyzed from the two pages of PEGASUS data (Leaman *et al.*, 1987), revealing agreement in the location of the maximum perturbation energy—that is, on the cyclonically-sheared side of the current just west of the core near the surface, and remaining associated with the west side of the current core with depth. The model exhibits a smaller perturbation energy maximum along the bottom topography eastward of the deepest point. This is also evident in the analysis of observations, though weakly, and may be due to the existence of bottom trapped waves, excited by the growing perturbation, or to the fact that $\delta_B < 0$ there.

In Section 2, we describe the numerical model and in Section 3 the development of the idealized initial conditions. Within the context of these conditions, we examine the current stability for the flat bottom channel and that with the 27N topography in Section 4. In the fifth, we detail the development of initial conditions from the STACS observational analysis and examine the stability of the more realistic current. In the final section, we summarize and qualify the results and briefly compare with De Szoeke's (1975) results.

2. The model and domain characteristics

a. The model. The numerical model used in this study is the isopycnic coordinate primitive equation model of Bleck and Boudra (1986). Such a model is particularly suited for this investigation because of the substantial baroclinicity associated with western boundary currents. Vertical resolution is, for instance, concentrated within the highly sheared part of the current core. In addition, the numerically required lateral diffusion is along isopycnal, rather than horizontal, surfaces. Conceptually, meanders and eddies, such as depicted in Figure 1 are optimally treated by the vertical coordinate system, which continually deforms to accommodate their baroclinic structure as they move downstream.

The advantages of the isopycnic coordinate system can be overwhelmed by numerical difficulties associated with isopycnal outcropping and intersection with bottom topography. As described by Bleck and Boudra (1986), referred to hereafter as BB, the model used here accommodates the collapsing of coordinate layers by use of a special algorithm, Flux-Corrected Transport (FCT) (Boris and Book, 1973; Zalesak, 1979), in integration of the mass continuity equation (the layer thickness tendency equation). In accordance with FCT, mass fluxes into and out of a grid box are tentatively calculated with a fourth-order scheme. If negative layer thicknesses would result, the high-order estimate is blended with that from an upstream, first order approximation. Zero thickness is allowed, but negative values are avoided. Because of the implicit diffusion associated with the upstream scheme, the solution is somewhat more diffusive at the edges of zero thickness regions than in the interior, but coordinate surface outcropping is made numerically tractable. For additional detail on incorporation of FCT into the model, the reader is referred to BB. For the current application, two additional numerical devices, related to the existence of zero layer thickness, have been incorporated and are described below.

For computational convenience, the model equations are integrated in full at grid points with zero as well as nonzero layer thickness. This is relatively trouble-free when coordinate interfaces do not merge with the lower boundary. The latter situation cannot be avoided, however, in the current problem, where the bottom topography, depicted in Figure 2, slopes steeply. In this case, if grid points in more than one massless layer coincide at the channel bottom, different values for the isopycnic gradient of the Montgomery Potential, $M = gz + p\alpha$, will be obtained at the bottom depending on which layer the gradient is evaluated in. The computation of the horizontal pressure force in the momentum equations at the bottom will thus be ambiguous. Following Bleck (1984), an unambiguous value is obtained by averaging the pressure force vertically over the bottom 30 m of real fluid, and the outcome is assigned to all layers confined within this distance from the bottom. The problem is not encountered at the upper boundary since $p\alpha$ is zero there.

The above safeguard apparently does not completely remove the possibility that the velocity values in massless regions can become noisy. To prevent this from having deleterious effects in the adjacent nonzero thickness regions, we have adopted a weighting of velocities which, at the end of each time step, replaces velocities at any grid point having less than 5 m layer thickness by a 5 m vertical average. In particular, massless grid points at the upper and lower boundary are reassigned velocities computed as a mean from the 5 m just below and above them, respectively.

b. Domain shape, boundary conditions, lateral friction. To study the stability of the Florida Current at 27N, the above model is configured in a north-south oriented channel with cyclic boundary conditions in that direction. Thus, two of the model's limitations with respect to reality are in its lack of regard for (1) downstream
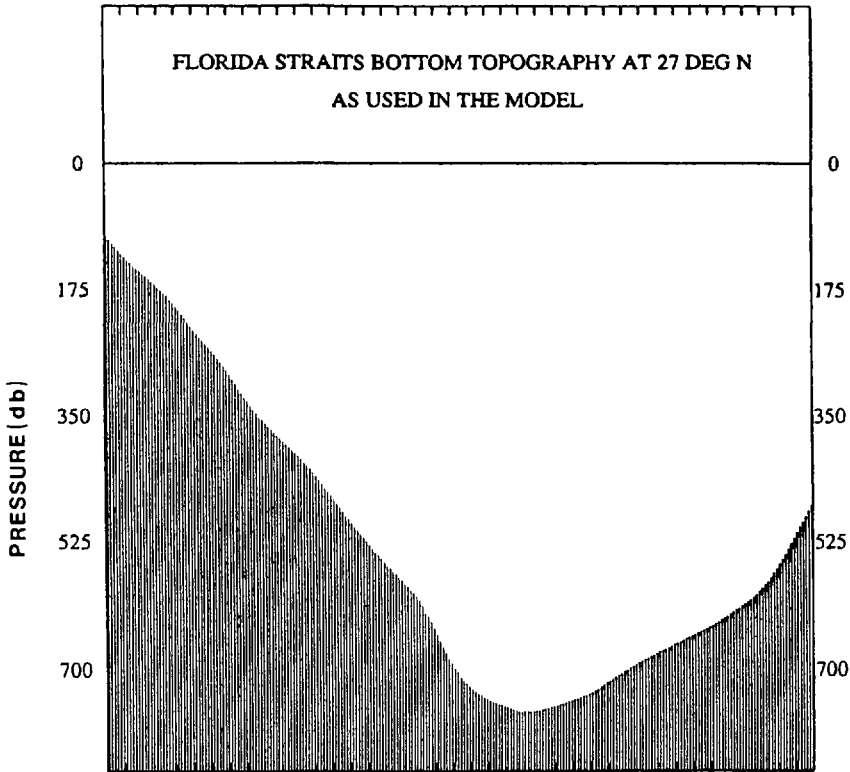
Figure 2. Representation of 27N bottom topography to be used in our experiments with topography. Total channel width is 78.8 km. Cross-channel grid-spacing is 1.878 km.

variations in channel geometry and (2) the actual amount of time which meanders spend in the Straits. Our results will be reviewed in light of these factors in the final discussion. The purpose here is to analyze the stability of the Current at the latitude of the STACS observations. It is deemed justified to ignore the latitudinal variation of Coriolis parameter because the latter changes very little within the Straits. In the experiments reported here, the model bottom is either (1) flat with a depth of 750 m or (2) of variable depth with the bathymetry of the Straits at 27N (Fig. 2). In the latter case, the extreme western and eastern sides of the channel are excluded, representing depths less than 100 m on the west and the almost vertical topography on the east. We should note that features such as shingles, associated with the western edges of spinoff eddies, are perhaps poorly represented due to the western exclusion. The channel width is 78.9 km. Cross-stream grid spacing is 1.878 km, the interpolation spacing used in the analysis of PEGASUS data by Leaman *et al.* (1987), so that there are 43 total grid points across the channel. Downstream grid spacing varies as a function of perturbation wavelength, with either 16 or 32 points resolving the wave. The vertical is

approximated in ten isopycnal layers with an increment of 0.4 kg m^{-3} between consecutive layers.

The east-west lateral boundary condition is no-slip. Botton friction is incorporated according to a standard bulk formula in a 25 m thick bottom boundary layer, using a quadratic drag coefficient of $C_d = 0.003$. Internal lateral friction in the equations of motion is of the monoharmonic type and takes into account the horizontal variation of layer thickness:

$$\left(\frac{\partial p}{\partial \rho}\right)^{-1} A_m \nabla \cdot \left(\frac{\partial p}{\partial \rho} \nabla (u, v)\right).$$

where A_m, the lateral viscosity, is 10 m^2 s^{-1}.

3. Idealized initial conditions

Our idealized initialization procedure, which may be employed to test the current stability as a function of several basic parameters, begins with an analytical function relating pressure and density:

$$
\begin{aligned}
p = -0.1 p_o \ln &\left(\frac{\alpha_{bot}/(1 - e^{-p_{bot}/p_o}) + \alpha_{hor} - \alpha}{\alpha_{bot}/(1 - e^{-p_{bot}/p_o}) + \alpha_{hor} \tanh (Bx)/\tanh (B)}\right) \\
-0.9 p_o \ln &\left(\frac{\alpha_{bot}/(1 - e^{-p_{bot}/p_o}) + \alpha_{hor}(1 - \tanh (Bx)/\tanh (B)) - \alpha}{\alpha_{bot}/(1 - e^{-p_{bot}/p_o})}\right)
\end{aligned}
$$

where $\alpha = \rho - 1000$ kg m^{-3}; $p_o = 300$ db, the vertical pressure scale; $p_{bot} = 800$ db, bottom pressure; $\alpha_{bot} = 4$ kg m^{-3}, top-to-bottom density scale (so that $0 \le \alpha \le \alpha_{bot}$); and x is the cross-stream direction $(-1 \le x \le 1)$. The function yields gently sloping isopycnals with an exponentially decreasing vertical variation of density with depth. The scale of the variation, p_o, is chosen so that much of it is placed within the upper 300 m, as is the case in the mean structure described in the STACS analysis (Leaman *et al.*, 1987). α_{bot} and p_{bot} represent the total top-to-bottom density and pressure variation and are easily extracted from the STACS analyses. An appropriate value for the parameter α_{hor}, representing the surface density variation across the Straits, is not as easily obtained. The data exhibit a nearly homogeneous surface layer varying from ≈ 30 m thickness on the western boundary to ≈ 70 m on the east, so that there is very little cross channel surface density gradient (≈ 0.2 kg m^{-3}). At 70 m depth, the increase from east to west is 1.4 kg m^{-3}. The value chosen for the experiments described here is 1 kg m^{-3}, corresponding to the actual value at 50 to 60 m depth.

The 'tanh' function in the above formula introduces at the desired cross-stream position a region of enhanced isopycnal slope, of which the magnitude is controlled by the parameter B, representing a frontal type feature near the surface. The observations (Leaman *et al.*, 1987) suggest that such a feature is located, in the mean, very close to

the western boundary, the location where it is placed here. Experimentation led to the choice $B = 7$.

Once the mass field has been specified in a single cross-section from this formula, a corresponding geostrophic downstream motion field is calculated. Since the above formula does not represent the asymmetries associated with finite amplitude fronts, a dynamical initialization is then carried out. The jet in the above weakly baroclinic state is 'spun up' by initially choosing the points $x = +1, -1$ to be ~450 km apart and by deforming the channel geometry in the course of time until the channel has reached the desired width, 78.9 km (Bleck *et al.*, 1988). Bringing the lateral side walls together essentially simulates the large-scale deformation process which, according to the theoretical work of Hoskins and Bretherton (1972), leads to a zero-order frontal discontinuity after a finite time. We carry out this deformation process in two dimensions; i.e., with all along-channel derivatives set to zero. While the resulting mass field has the desired frontal structure, the jet development lags behind the geostrophic current implied by the mass field. Therefore, a new geostrophic motion field is computed following the deformation phase.

At this point, the lateral and bottom boundary conditions are applied, and in the case of variable bottom topography, the bathymetry is incorporated. The dynamical fields must then be allowed to adjust to the boundary conditions so that the initial mass and downstream flow fields for the stability experiments will be in balance. Thus, the single cross-section is integrated forward, now with constant channel width, for several more days. At the beginning of this integration, the total transport through the cross-section is brought up to its realistic value by addition of a uniform downstream velocity over the cross-section. This transport, 31.7×10^6 m^3 s^{-1} (Leaman *et al.*, 1987), is held constant throughout the experiments, which is justified here by Johns and Schott's (1987) finding that transport fluctuations are relatively uncorrelated with meanders. During the last few days of the integration, the mass and downstream flow fields for each time step are averaged together to produce a balanced data set. This effectively removes oscillations with periods of as much as a few days. As we shall see in a moment, however, long term trends associated with slow adjustment of the mass/flow field to the boundary conditions may still be present. Near the end of this dynamical initialization, a cross-stream motion field is saved. This field represents motion involved in adjustment to the boundary conditions and provides the amplitude of a function varying sinusoidally in the downstream direction, to be used subsequently as the small initial perturbation needed to test for stability.

4. Current stability with idealized initial structure

a. Flat bottom channel. To provide a reference point for the effect of the 27N bottom topography, we first present results for a flat bottom channel initialized in the above
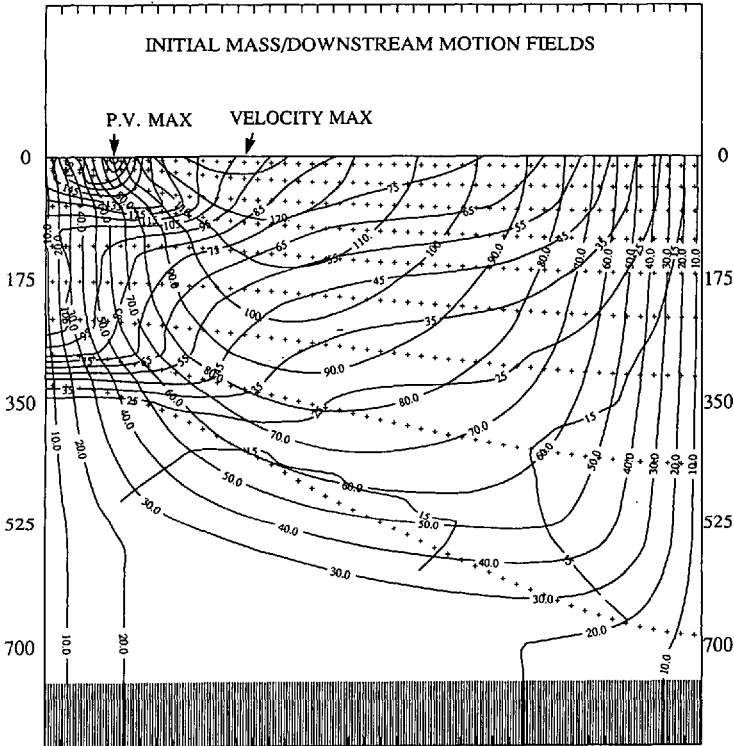
Figure 3. Initial mass and downstream velocity fields for the flat bottom experiments. The isopycnal layer interfaces are indicated by rows of 'plus' signs. Northward velocity is contoured at 10 cm s^{-1} intervals and contour labels include a decimal point. Potential vorticity (PV), $((\partial v/\partial x)_p + f)\partial\rho/\partial p + \partial v/\partial p(\partial\rho/\partial x)_p$, is superimposed and is contoured in intervals of 1×10^{-15} cm^{-2} s. PV contour labels include no decimal point.

fashion. The initial fields for the flat bottom experiments are illustrated in Figure 3. The potential vorticity (PV) field, $((\partial v/\partial x)_p + f) \partial\rho/\partial p + \partial v/\partial p (\partial\rho/ \partial x)_p$, superimposed on the mass and downstream flow fields in the figure, is generally characterized by values which increase from bottom to top and from east to west. Exceptions are found near and west of the surface current core and below 350 m where the PV gradient is much weaker. The general quasi-geostrophic (QG) necessary condition for instability is that the isentropic (which is equivalent to *isopycnal* in our model) potential vorticity (IPV) gradient change sign somewhere in the cross-section (see, e.g., Pedlosky, 1987). Reversals in the IPV gradient along isopycnals are associated with barotropic instability (Charney and Stern, 1962), and vertical reversals are associated with baroclinic instability (Pedlosky, 1987). In Figure 3, looking along isopycnals, the IPV gradient changes sign in the lower right and left between 350 and 600 m (though weakly) and also near the surface on the west side. Thus, the QG necessary condition for barotropic instability is met. The vertical reversal (necessary condition for
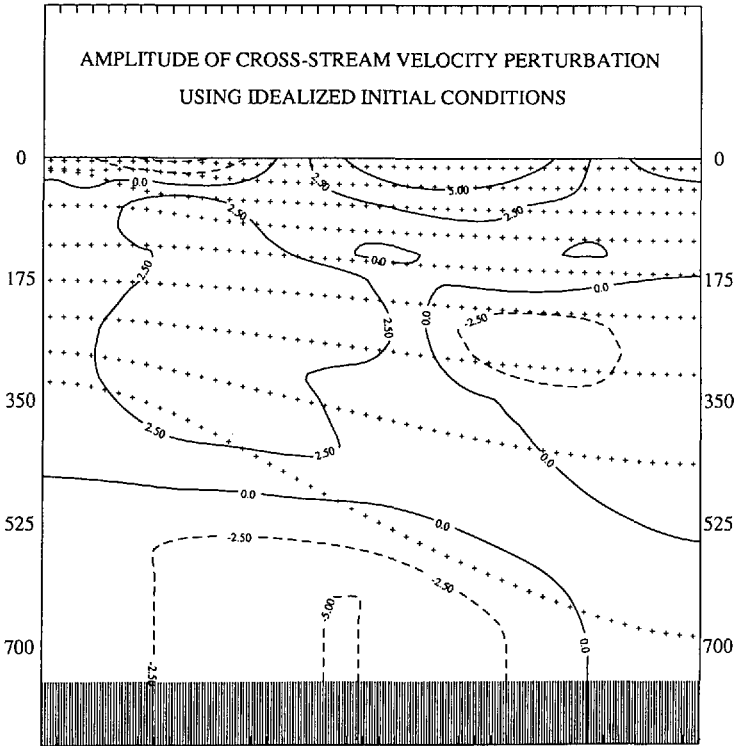
Figure 4. Cross-stream velocity field used as amplitude of the initial perturbation varying sinusoidally downstream. Contour intervals is 2.5 cm s^{-1}. Isopycnal interfaces are indicated as in Figure 3.

baroclinic instability) happens in the lower half of the cross-section, where the gradient is weak, and once again, above 175 m to the west of the surface current core, where the IPV gradient is very strong. Thus, necessary conditions for both barotropic and baroclinic instability are present in these initial conditions. Necessary conditions related to the upper and lower boundaries, requiring temperature gradients along these boundaries (Charney and Stern, 1962) are apparently not met in this cross-section, as the density is uniform along each (although the uppermost isopycnal almost outcrops in the upper left).

The amplitude of the sinusoidal downstream perturbation in the cross-stream velocity for the flat bottom experiments is illustrated in Figure 4. The *X-Z* structure of this perturbation is apparently complex, but is felt to be sufficiently arbitrary and of small enough amplitude to qualify as the small perturbation needed to test the stability of the current. Maximum values are of order 5 cm s^{-1} at the top and bottom and are smaller in the interior. For the flat bottom experiments, the downstream sinusoidal structure is resolved by 16 grid points.

Table 1. Perturbation energy and baroclinic conversion $(P \rightarrow K_e)$ maxima as a function of wavelength for flat bottom channel experiments, vertically integrated and averaged over the channel. Energies are in 10^3 J m^{-2}, Conversion in W m^{-2}, Time in Days.

λ (km)	60	90	120	150	180	210	240
$(K_e)_{max}$	.15	14.8	27.6	41.6	46.4	41.6	34.2
Time	0	20	14.5	18.0	21.1	24.3	31.2
$(K_e + P_e)_{max}$	.17	17.4	31.5	49.8	60.3	57.0	50.0
Time	.4	20	14.1	18	21.1	24.3	31.2
$(P \rightarrow K_e)_{max}$	.001	.092	.175	.22	.198	.21	.156
Time	0	18.2	11.7	14.0	18.0	23.1	27

As suggested above, our method of examining the stability of the model Florida Current is within the context of individual perturbation wavelength experiments. Alternatively, or as a complement, one might test the stability of the current to a perturbation of arbitrary downstream structure in a very long channel, the method of Orlanski and Cox (1973) in their model of instabilities in the Gulf Stream off the Carolinas. In fact, such experiments have been run and some results will be presented in the concluding section.

The stability of the current to perturbation wavelengths from 60 km up to 240 km has been tested, at intervals of 30 km. Some of the growth statistics are given in Table 1. It is seen there that the perturbation reaching maximum energy (dominated by the perturbation kinetic energy) has $\lambda = 180$ km, corresponding to a period of approximately 5 days. The 60 km perturbation grows not at all (in fact, decays) and the $\lambda = 90$ km perturbation is apparently near the short wavelength cutoff, so that it grows very slowly up to about 15 days and then remains neutral. Above 90 km the time required to reach maximum perturbation energy increases with wavelength.

To conserve space we focus attention on the 180 km perturbation for the remainder of our analysis. The mean and eddy potential and kinetic energies as a function of time for the $\lambda = 180$ km perturbation are shown in Figure 5. Here, the mean energies are defined as those associated with the along-channel mean mass/flow structure, and the eddy energy is defined as the total energy minus the mean. We first note that the mean potential energy is slowly increasing during the first 12 days of this experiment. This is due to a slow adjustment of the mass/flow structure to the boundary conditions. Energy is imparted to the current by the above-mentioned requirement that the total mass transport remain constant in time. This energy source works against the dissipative forces of lateral (internal and sidewall) and bottom friction, and can be equated to an alongstream pressure head in the Straits of Florida. A diagnostic calculation in our experiments (relating the applied acceleration to an along-channel pressure gradient) suggests that such a pressure head would be yielded by a downstream sea surface tilt of approximately 1 cm/km initially, and two to three times that slope when meanders develop significant amplitude. This is considerably larger than the downstream slope which actually exists in the Straits of Florida, but diagnosis
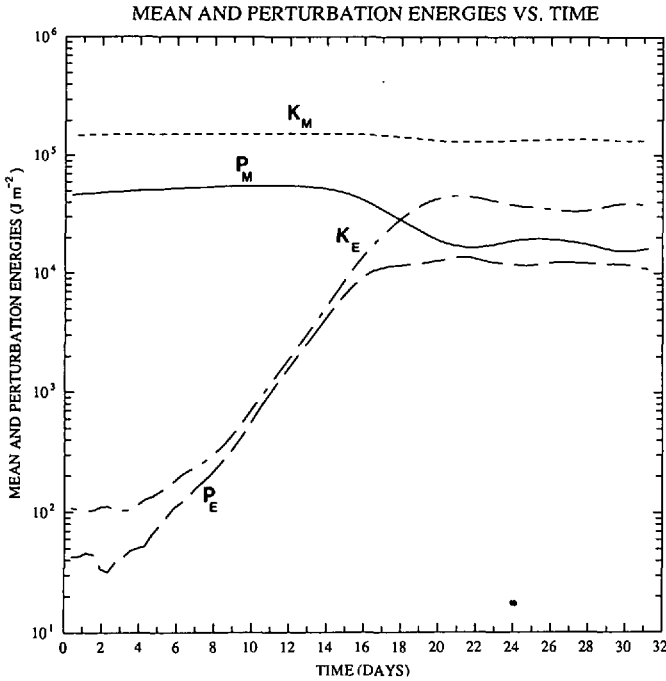
MEAN AND PERTURBATION ENERGIES VS. TIME

Figure 5. Time-series vertically integrated and channel-averaged mean (M) and perturbation (E) kinetic (K) and available potential (P) energies for the indicated experiment.

of such a parameter provides a convenient frame of reference for gauging the resistance which internal and boundary friction exert on the model current. The transport boundary condition is a direct source of kinetic energy, since it works against dissipation, but some of this is converted to available potential energy. The primary mechanism for the increase in P_m is the spin-down of the flow next to the bottom in response to the quadratic bottom friction. Since total transport is held constant, this leads to increased slope of the isopycnals and, thus, more available potential energy.

The perturbation potential and kinetic energies are initially three orders of magnitude smaller than the means and begin to increase, at first very slowly, 4 days into the experiment (Fig. 5). It is presumed that some initial amount of time is required in which the perturbation (Fig. 4) becomes suitably organized to begin drawing energy from the mean flow. Both perturbation energies accelerate their growth then until day 17, when P_e levels off. Between days 9 and 16 their growth is exponential, as might be predicted by linear theory. At 12 days, the P_m begins to decrease and falls to one third of its original value by day 21. K_e continues to increase to day 21, when it is 2.5 times as large as P_m. P_e remains almost constant from day 16 to 21, apparently because here P_m is being converted to P_e only as rapidly as P_e is then being given up to K_e, i.e., the transfer from P_m to K_e has become very efficient at this stage. During the period day 12

A) INITIAL, UPPER 30 M FLOW FIELD   B) UPPER 30 M FLOW FIELD, DAY 20.8

180 KM PERTURBATION
FLAT BOTTOM

USING IDEALIZED
INITIAL CONDITIONS

180 KM PERTURBATION
FLAT BOTTOM
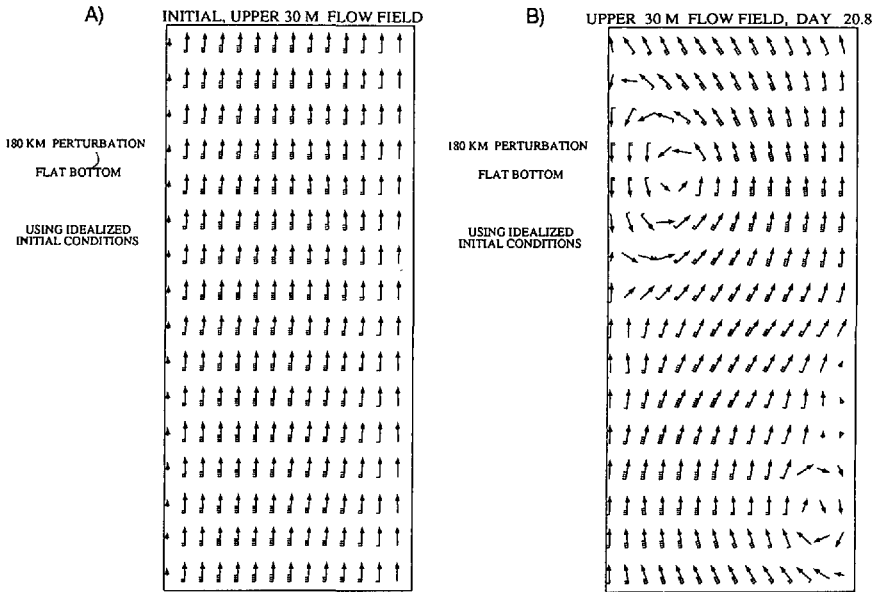
USING IDEALIZED
INITIAL CONDITIONS

Figure 6. Velocity field averaged over the upper 30 m (a) near the initial time and (b) near the time of maximum K_E for the $\lambda = 180$ km perturbation flat bottom experiment. Velocities are indicated for each grid point in the along-channel direction and for every third grid point across the channel. A full-length arrow and each additional barb represent 25 cm s^{-1} in flow speed.

to 21, then, the mean structure of the current has been substantially changed, and since it is the mean potential energy which has been depleted while the perturbation energy has increased, the physical mechanism is likely the release of baroclinic instability. In a moment, we will examine the mean-eddy energy conversions to verify this hypothesis. After day 21, the energies oscillate with small amplitude about the levels achieved during the previous period, but show no tendency toward further substantial changes. These perturbation energy curves exhibit characteristics of both the inviscid and the strongly viscous systems for which Pedlosky (1987) describes behavior due to nonlinear baroclinic instability, suggesting that the parameters chosen here correspond to an intermediate friction case. Once neutral stability has been reached, the inviscid system exhibits rather high amplitude oscillations about it, and the highly viscous system, assumed to have a continual energy source, becomes steady. In our *intermediate* case, the energy source is the requirement that total transport remain constant with time, and the frictional sink is mainly the bottom boundary layer.

The change in the flow pattern resulting from this perturbation growth is illustrated in Figure 6, where the velocity distribution averaged over the upper 30 m, both at the initial time and near the peak amplitude of the perturbation, are shown. Barely perceptible initially (Fig. 6a), the meander dominates the channel flow pattern in
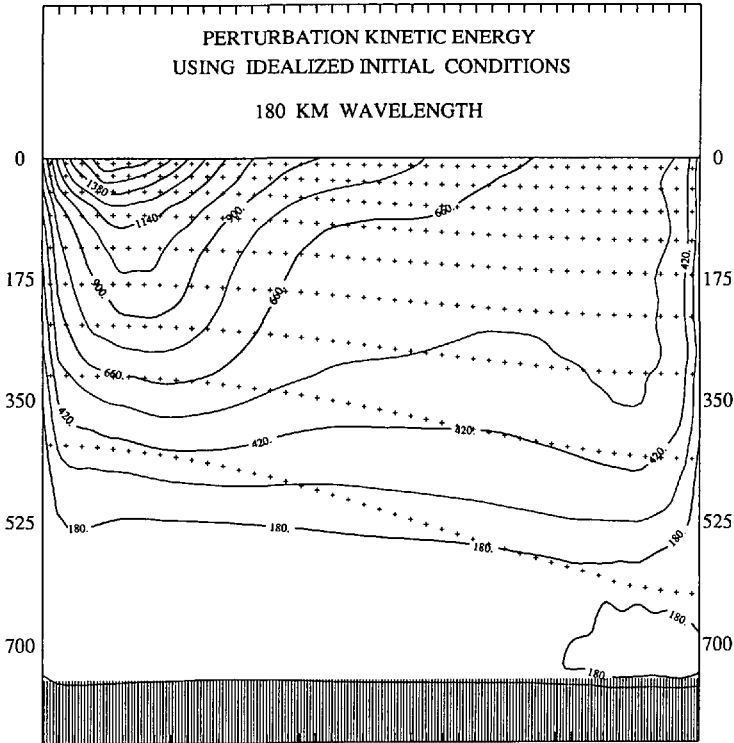
Figure 7. Cross-section of perturbation kinetic energy for the few days period surrounding the time of maximum K_E. Contoured units are .1 J m^{-3} and the contour interval is 12 J m^{-3} The downstream mean positions of the isopycnal interfaces are indicated.

Figure 6b, and a striking eddy moves downstream in the cyclonically curved portion of the wave. The eddy has a diameter of about 54 km, twice the size of that shown in Figure 1 and much larger than any eddy known to have been observed in the Straits of Florida. A small clockwise eddy has also formed in the anticyclonically curved portion of the meander along the eastern boundary. The high amplitude leading to the closed circulations suggests that nonlinear effects are important at this time and likely during the few days period before maximum amplitude is reached.

The cross-sectional structure of the perturbation, illustrated here in the perturbation kinetic energy (Fig. 7), exhibits maximum intensity near the surface and west of the current core, with a tongue of high perturbation energy extending downward from there along the cyclonically sheared side of the current. This primary maximum is in a region identified as possessing necessary conditions for both barotropic and baroclinic instability in the initial conditions. A secondary local maximum in the deep part of the channel is found in the eastern half, where the initial IPV gradient also reversed signs both in the horizontal and vertical. K_e over the remainder of the cross-section is far

from negligible, however, confirming the fact that the meander flow pattern occupies the entire channel, while its amplitude decreases with depth.

To verify the apparent importance of release of baroclinic instability in the meander growth, we examine the energy conversion terms, corresponding to baroclinic conversion $(P \rightarrow K_e)$, barotropic conversion $(K_m \rightarrow K_e)$ and conversion between potential and mean kinetic energy $(P \rightarrow K_m)$, for the $\lambda = 180$ km perturbation experiment as a function of time (Fig. 8). Bleck (1985) derived the energy conversion terms appropriate for isopycnic coordinates. In an intercomparison of isopycnic, quasi-isopycnic, and isobaric coordinate models, BB found a slight incompatibility in the way eddy potential energy is defined in isopycnic and isobaric coordinate models and avoided distinguishing between mean and eddy potential energy in the conversions. While we define and illustrate the eddy potential energy above, we choose to lump the mean and eddy potential energies together so far as energy conversions are concerned, especially since the division is unnecessary in order to identify the physical mechanism of instability. The conversion terms have the form,

$$P \rightarrow K_e = -\mathbf{v}' \cdot \frac{\partial p}{\partial \rho} \nabla_\rho M$$

$$P \rightarrow K_m = -\tilde{\mathbf{v}} \cdot \frac{\partial p}{\partial \rho} \nabla_\rho M$$

$$K_e \rightarrow K_m = \mathbf{v}' \frac{\partial p}{\partial \rho} \cdot (\mathbf{v}' \cdot \nabla_\rho)\tilde{\mathbf{v}}$$

where M is Montgomery Potential, ($\tilde{\ }$) is the along-stream mass-weighted average, and ( )′ is the departure from ($\tilde{\ }$). In Figure 8, we see that initially the total potential to kinetic energy conversion is in the direction of mean kinetic energy and is steady. P is converted to K_m which is lost through the model dissipative processes, mainly at the boundaries. The fact that there is very little oscillation suggests that the mass and downstream flow fields are well-balanced with each other and are simply evolving slowly in response to frictional effects. The conversions involving K_e are negligible and remain so until day 5, at which time baroclinic conversion slowly rises and barotropic conversion falls below zero. By day 14, baroclinic conversion is rising sharply—that is, P is being transferred to K_e more and more rapidly—and the K_e is being lost to K_m, but at a much slower rate. In addition, because P is being transferred so rapidly to K_e, a transfer from K_m to P is initiated. Because of the rapid conversion of P to K_e, the mass and flow fields are no longer well-balanced, and an oscillation in the conversion between P and K_m is initiated.

A peak in the vertically integrated and channel averaged baroclinic conversion of 0.2 watts m^{-2} is reached at 18 days, with a corresponding maximum of about 0.06 watts m^{-2} in negative barotropic conversion. Both of these decrease rapidly in magnitude over the next four days, but the net conversion to eddy kinetic energy
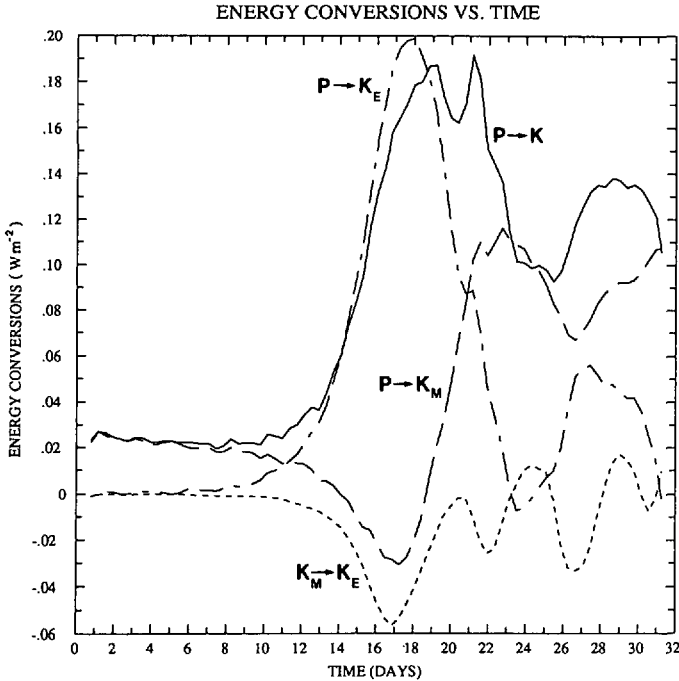
ENERGY CONVERSIONS VS. TIME

Figure 8. Time-series vertically integrated and channel-averaged energy conversion terms for the indicated experiment. Note that $P \rightarrow K_E$, and $K_M \rightarrow K_E$ represent baroclinic and barotropic conversion from the mean flow to the eddies, respectively.

remains positive through this period, so that the maximum K_e is achieved at ~day 21. As $P \rightarrow K_e$ is falling sharply from day 18 to day 23, $P \rightarrow K_m$ is rising, which tends to stabilize the flow (in the baroclinic sense). Then as the potential to mean kinetic energy conversion falls off, $P \rightarrow K_e$ rises again, though not nearly so much as with the initial release of instability. Dissipation (not shown) is apparently of minor importance in these growth cycles since K_e (Fig. 5) responds primarily to the combination of $P \rightarrow K_e$ and $K_m \rightarrow K_e$ (Fig. 8). And yet friction is strong enough that the oscillations in P_m and K_e following release of the major instability are of relatively low amplitude, that is, compared to those which might be expected in the inviscid case for nonlinear instability (Pedlosky, 1987).

From the above, it is apparent that a current in a flat bottom channel, initialized with the same basic parameters as exist in the Florida Current at 27N, is unstable. And while the initial PV structure of the current is such that necessary conditions for both barotropic and baroclinic instability are apparently met, the large positive baroclinic and negative barotropic energy conversion during perturbation growth leave little doubt here that the physical mechanism of amplification is release of baroclinic
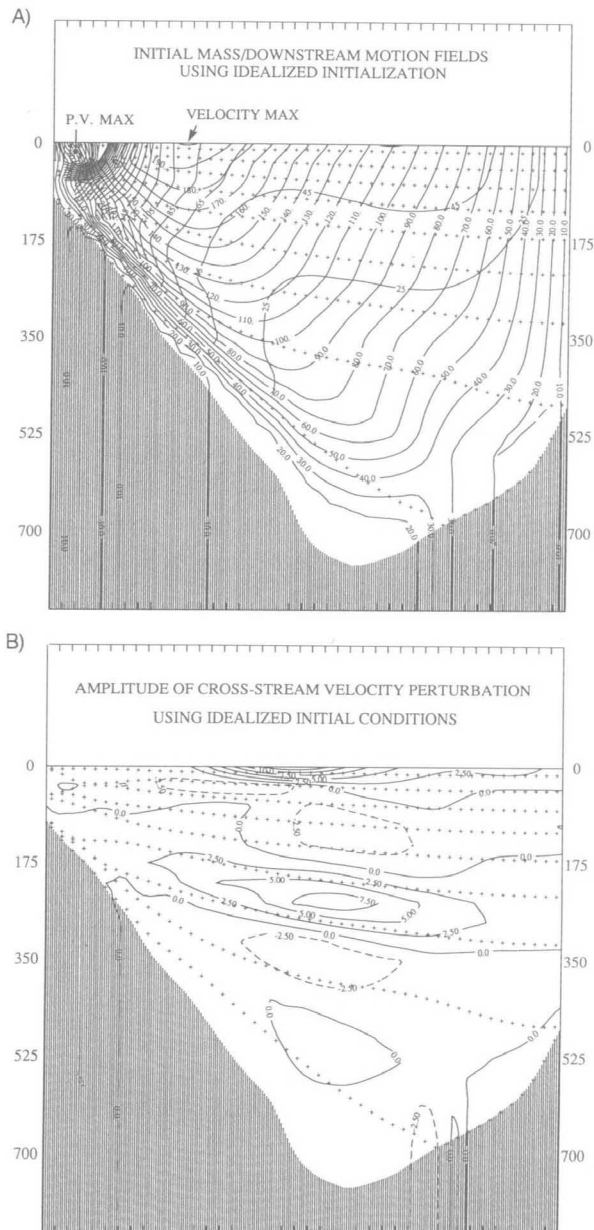
Figure 9. (a) As in Figure 3 for the $\lambda = 180$ km perturbation experiment and using the 27N bottom topography. Potential vorticity is contoured at intervals of 2×10^{-15} cm^{-2} s. Note the change in sign in the potential vorticity gradient along isopycnal surfaces to the left of the surface current core. (b) As in Figure 4 for the same experiment as (a).

instability. In what follows, results from these flat bottom experiments will be helpful in interpreting the influence of the 27N topography.

b. Channel with 27N topography. The initial conditions for experiments with the Straits bottom topography, developed in the manner described in Section 3 are illustrated in Figure 9. Other than the intrinsic difference due to the fact that bottom topography substantially reduces the amount of fluid in the channel, the primary differences in the dynamical structure are along the sloping topography on the channel's west side. Downstream velocities are generally greater than in the case with a flat bottom; for instance, in the latter, the surface current core maximum is $130+$ cm s^{-1} and here it is $190+$ cm s^{-1}, so that both horizontal and vertical shears are also greater. The increase is due to the much reduced cross-sectional area which must transport the same amount of fluid. One result is that the PV maximum to the west of the current core is much larger. Associated with this maximum is, as in the flat bottom case, a QG necessary condition for barotropic instability. And the associated vertical change in the sign of the IPV gradient qualifies as a necessary condition for baroclinic instability. A maximum in potential vorticity also lies along the western slope, apparently associated with the thinning of the isopycnal layers in the upslope direction. A change in the sign of the gradient is not present here. Neither is there a change in sign in the lower right portion of the cross-section, such as was present in the flat bottom case. Also in contrast to the flat bottom case, a density gradient along the channel bottom is implied here by the merging of the deepest layer interface with the bottom topography at ~ 200 m on the west side and 700 m on the east. Necessary conditions for instability associated with the lower boundary may thus exist. Several authors (e.g., Blumsack and Gierasch, 1972; Orlanski and Cox, 1973; De Szoeke, 1975; Mechoso, 1980; Pedlosky, 1964, 1987; Johns, 1988) have pointed out that if the deep isopycnals slope upward less steeply to the left looking downstream than the bottom ($\delta_B > 1$, then the effect of the bottom topography is to stabilize the flow. This is the case on the west side of our cross-section and, thus, the existence of a density gradient along the bottom there does not qualify as a necessary condition for instability. Since this is normally the case for the Gulf Stream along the U. S. coast, the bottom topography there is generally felt to have a stabilizing effect on the current. The channel-like geometry of the Florida Straits, on the other hand, offers the possibility seen in the lower right of Figure 9—namely, that the deep isopycnals may come together with the eastern topography in a fashion which may destabilize the flow (Blumsack and Gierasch, 1972; Mechoso, 1980). In fact, it is with this condition, in which $\delta_B < 0$, that De Szoeke (1975) demonstrated that his *hybrid* baroclinic instabilities are most likely in the Florida Straits. In a two-layer model, Pedlosky (1964) showed that for instability to exist, δ_B must be less than 1. Although our model has ten layers, the equivalent condition is located eastward of the deepest part of the channel in our initial conditions. We thus have both internal and lower boundary

Table 2. As in Table 1 for experiments using the theoretically-based initial conditions in a channel with 27N bottom topography.

λ (km)	60	90	120	150	165	180	195	210	240
$(K_e)_{max}$	1.2	9.5	10.8	9.7	12.1	13.0	10.3	9.9	9.0
Time	16.4	21.1	26.6	28.6	29.8	37.6	20.4	25.5	21.1
$(K_e + P_e)_{max}$	1.67	12.5	13.86	12.5	16.25	17.4	13.26	13.18	11.6
Time	16.4	21.1	26.6	29.0	29.4	37.6	21.5	25.5	21.5
$(P \rightarrow K_e)_{max}$	.009	.056	.078	.044	.06	.08	.057	.058	.045
Time	18.0	25.2	25.5	26.6	26.6	36.9	17.6	24.7	27.0

configurations suggesting that QG necessary conditions for baroclinic instability are met.

The amplitude of the initial cross-stream velocity perturbation (Fig. 9b) has maximum values as large as 15 cm s^{-1} at mid-channel in the uppermost layer and 10 cm s^{-1} at mid-depth. It is, however, very small over the greatest portion of the cross-sectional area.

Results of our experiments with bottom topography proved to be more sensitive to downstream resolution than with a flat bottom. This is apparently because interactions among the wavelength initially specified, the mean flow, and curvature of the bottom topography produce a more complex downstream structure than obtained with a flat bottom. This process is central to De Szoeke's (1975) theory of *modified Eady* and *hybrid* baroclinic instabilities and has a strong impact here. Because of the resulting sensitivity to resolution, all experiments presented here and in the next section resolve the sinusoidal downstream structure with 32 as opposed to 16 grid points. We address this issue again shortly.

Once again the stability of the current is tested as a function of perturbation wavelength from 60 up to 240 km. Table 2 summarizes the results in terms of maximum K_e, $K_e + P_e$, and $P \rightarrow K_e$ values and the time of each. In this case, the 60 km perturbation appears to be closer to the short wavelength cutoff, as it amplifies slightly and in the previous case only decayed. Introduction of bottom topography has therefore slightly destablized the current with respect to shorter wavelengths.[3] If we compare Tables 1 and 2, we immediately note that, for perturbation wavelengths of 90 km and above, the maximum eddy energies are greatly reduced by the topography. The maximum energies and baroclinic conversion rates are reached once again for $\lambda = 180$ km (in this case, with a period of a little more than four days), but the maximum values are less than one-third those obtained with a flat bottom. In addition, considerably more time is required for the meanders to reach their maximum amplitude. Also, a preliminary K_e maximum is reached for $\lambda = 120$ km, and throughout the wavelength band from 90 km to 240 km the maximum amplitudes

3. As demonstrated by Blumsack and Gierasch (1972) and Mechoso (1980) for a two-layer model, this is most likely due to the negative value of δ_g east of the deepest point in the channel.

differ only by ~30%. In the cases, $\lambda > 180$ km, perturbations with half the wavelength of the initially specified one are generated, apparently due to interaction with the bottom topography variation (De Szoeke, 1975). Since these shorter wavelengths draw energy more efficiently and quickly from the mean flow than those initially specified, they amplify earlier in the experiments and their maximum amplitudes are reached much earlier than for the 180 km wavelength. Hereafter, we refer to these shorter wavelengths as the *half-wavelength harmonics* of the initially specified perturbation. In general, comparing Tables 1 and 2, we form the impression that the bottom topography suppresses the instability over most of the wavenumber range, as is generally the case (e.g., see Orlanski and Cox, 1973; Pedlosky, 1964, 1987; Johns, 1988), but slightly destabilizes perturbations close to the short wavelength cutoff.

To analyze the mechanisms of instability in this case, we again focus attention on mean-eddy energetics for the $\lambda = 180$ km experiment (Fig. 10). The curves are strikingly different from those for the same wavelength flat bottom experiment (Figs. 5 and 8). The mean kinetic energy is almost constant throughout the experiment and the mean potential energy slowly increases from 1.07 to 1.34×10^5 J m^{-2}. As in the flat bottom case, the increase is due to a slow adjustment of the mass/flow structure to the boundary conditions. While the perturbation energies increase, slowly up to 9 days and more rapidly thereafter, the maximum total perturbation energy is approximately an order of magnitude smaller than the mean potential energy. Moreover, it is more difficult to identify periods during which the growth is exponential, although two short such periods may be centered around days 12 and 18. The perturbation growth occurs in three bursts, near 17, 27, and 36 days, but a noticeable dip in P_m is associated only with the final event, contrasting sharply with the large drop in P_m in the flat bottom case.

The graph of energy conversions (Fig. 10b) is somewhat simplified from that shown for the flat bottom experiment in that it gives only the barotropic and baroclinic conversions and their sum, which is the net conversion of energy to K_e. The three primary events of meander growth and a final weaker one are easily identified in that sum, represented by the solid curve. The baroclinic conversion clearly dominates each growth event although we should note that each of the first two events are associated with weak barotropic conversion to the meander. Indeed, the barotropic conversion is the first to rise significantly above zero (at ~12 days), although it is quickly overtaken by the baroclinic conversion. Only the third and fourth events have the same clear signature of release of baroclinic instability as seen in the flat bottom case—that is, positive baroclinic conversion accompanied by negative barotropic conversion. The multiple event structure to the meander growth is a general characteristic of all the experiments with bottom topography, each growth period lasting for 3 to 4 days, followed by a somewhat longer decay period. It should also be noted that K_e dissipation (not shown) is apparently of some importance here since the sum of barotropic and baroclinic conversion remains above zero even when K_e is decreasing, except in the last

A)

MEAN AND PERTURBATION ENERGIES VS. TIME
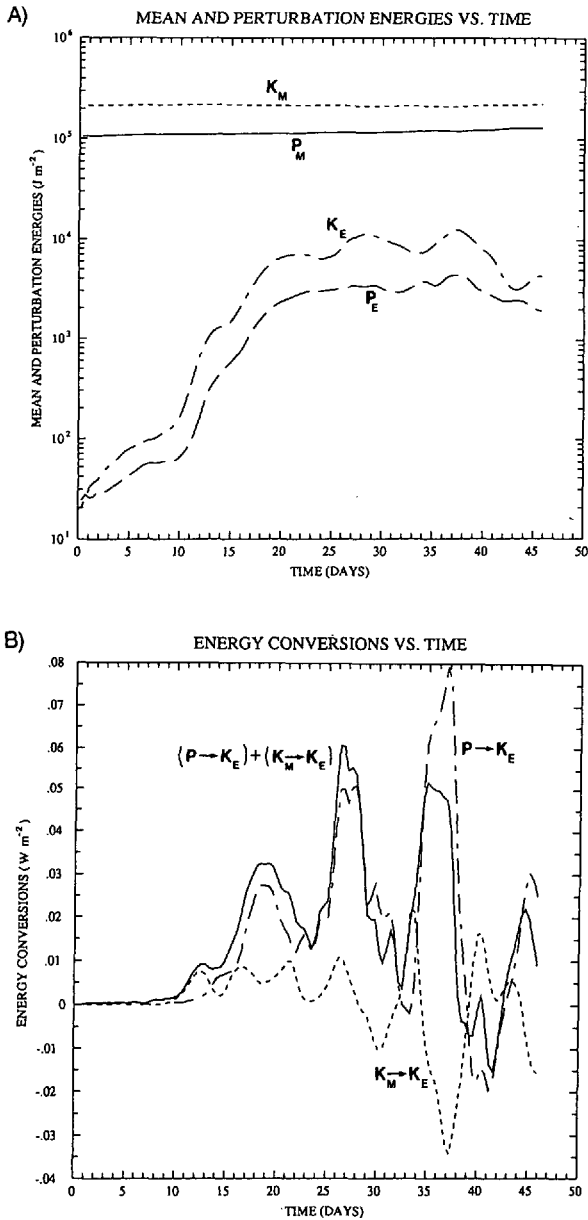

B)

ENERGY CONVERSIONS VS. TIME

Figure 10. As in Figure 5 for the $\lambda = 180$ km experiment with bottom topography and using idealized initial conditions. (b) As in Figure 8 for the same experiment as (a), except that a curve for the sum of barotropic and baroclinic conversion is substituted for $P \rightarrow K$, and the $P \rightarrow K_M$ curve has been deleted.

dropoff, from Day 38 to 44. The energetic behavior again is reminiscent of what one would expect in the nonlinear release of baroclinic instability for an intermediate level of friction (neither inviscid nor strongly fricitonal) (Pedlosky, 1987). In the lulls between the growth phases, dominated by surges in $P \rightarrow K_e$, K_e falls due primarily to friction and conversion to K_m and, in the final instance, to conversion back to P.

Summarizing, while positive barotropic conversion plays more of a role here than in the flat bottom case, the peaks in perturbation energy are clearly associated with those in baroclinic conversion. Release of barotropic instability might be considered the initiator of wave growth since $K_m \rightarrow K_e$ is the first conversion to rise above zero. But the primary physical mechanism of meander growth is, once again, release of baroclinic instability.

The much more limited character of the instability here than in the flat bottom case is confirmed by comparing the flow patterns near the time of maximum K_e, Figures 6b and 11a. In Figure 11a and the corresponding perturbation flow field (Fig. 11b), the meandering flow pattern can be detected across the entire channel, but in other respects the difference with Figure 6b is enormous. In particular, it seems that nonlinear effects, in some sense, play a less important role in the meander behavior. Still, there is a reversing flow next to the western boundary, closing a cyclonic eddy, which has a diameter of ~15 km. As reported by Schmitz and Richardson (1968) and Johns and Schott (1987) Florida Current meanders at 27N generally have amplitudes of 3 to 5 km. That depicted in Figure 11 with amplitude of 7 to 8 km, thus, appears to be somewhat larger than those typically observed at that latitude, though it is smaller
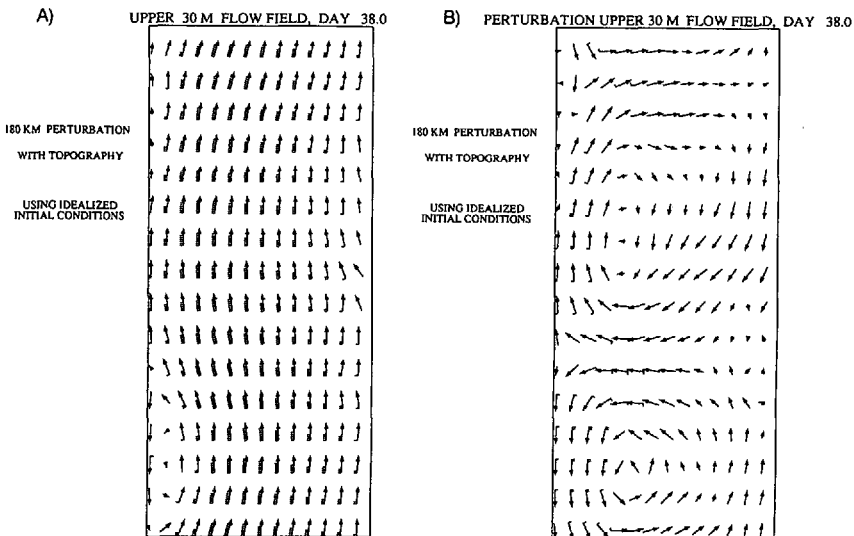

Figure 11. Mean total and perturbation upper 30 m flow field near the time of maximum K_E for the $\lambda = 180$ km perturbation experiment with bottom topography and using idealized initial conditions.

and less energetic than that depicted in Figure 1, which is centered at 26N. We should point out, however, that, due to engineering constraints on mooring design, Johns and Schott's (1987) measurements excluded the upper 150 m of the water column, where a substantial portion of the model perturbation energy is concentrated—that is, to the left of the current core (Fig. 12). The amplitudes in their analysis may, therefore, not be representative of those in the surface layer shown here (Fig. 11). Their numbers also represent root-mean-square amplitude estimates, so that significantly larger amplitude meanders may (and occasionally do) occur.

The mean K_e cross-section for the few days period surrounding the final energy maximum at 37.6 days is displayed in Figure 12(a). In addition to the maximum just west of the surface current core, where the IPV gradient in the initial conditions reversed signs (Fig. 9a), a tongue of maximum energy extends for some distance down along the sloping topography. Over the eastern two-thirds of the cross-section, the K_e is relatively small and the gradient weak, with two local maxima near the bottom of the channel.

A measure of the degree to which the model is producing the sort of meanders which occur in the Straits of Florida can be obtained by comparing our K_e cross-section with that analyzed by Leaman *et al.* (1987) for all the fluctuations observed during the STACS PEGASUS cruises in 1982–84 (Fig. 12b). In some respects, there is a remarkable degree of similarity between these two cross-sections, especially in the placement of the high K_e region and the weakness of the gradient over the remainder of the section. It should be pointed out, however, that details of the model perturbation energy cross-section exhibit a good deal of variation for different wavelengths and for different times during each experiment. The pattern shown in Figure 12a exhibits the best agreement we have seen with that shown in Figure 12b and appears to verify that the structure of the fully grown perturbation in this experiment is similar to those present in the Straits during the STACS cruises.

Finally, it was mentioned in the Introduction that the flow is at least marginally unstable in the current case when the cross-stream density variation is large enough. It is appropriate to note here that when the parameter α_{hor}, the east-to-west surface density scale in the initial specification of density as a function of pressure, is set to less than 0.3 kg m^{-3}, negligible amplification is incurred. As indicated in Section 3, the parameter value[4] chosen for the experiments in this section, 1 kg m^{-3}, is equal to the cross-stream horizontal density change at 50 to 60 m depth in the mean cross-section analyzed from PEGASUS data (Leaman *et al.,* 1987). Since the cross-stream density gradient is related to the vertical shear and thus to the baroclinicity of the current through the thermal wind, if a larger value is chosen for α_{hor}, the resulting current would likely be more baroclinically unstable and more wave amplification could be expected.

---

4. The same value was used by De Szoeke (1975) in application of his theory of *modified Eady* and *hybrid* topographic baroclinic instabilities to the Straits.

A)

PERTURBATION KINETIC ENERGY
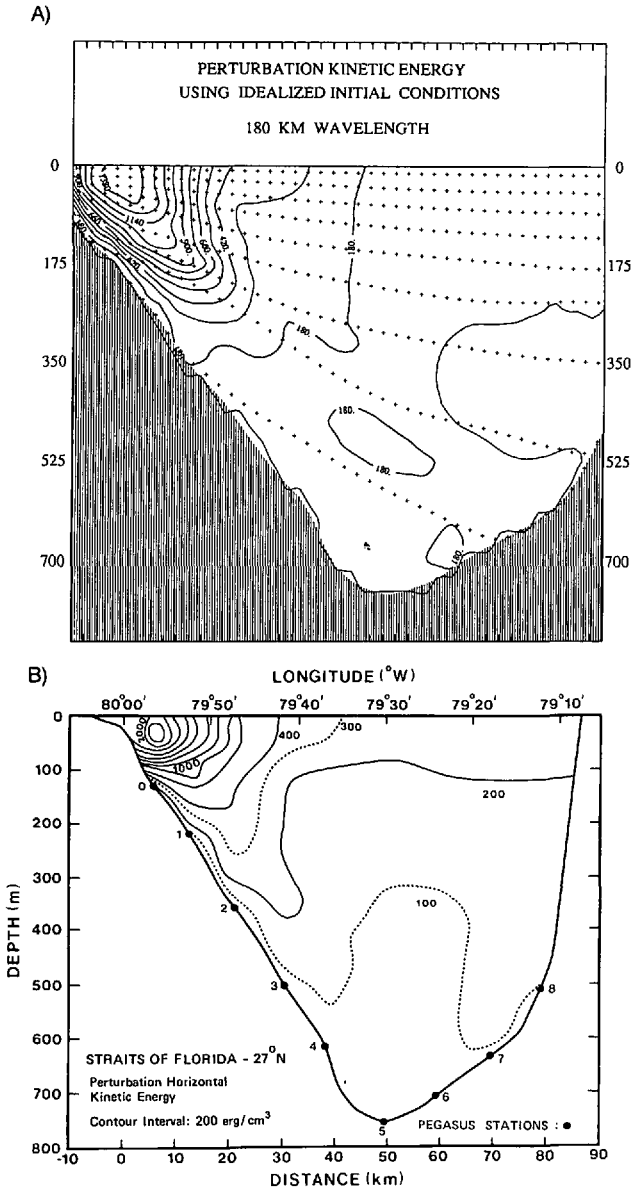USING IDEALIZED INITIAL CONDITIONS

180 KM WAVELENGTH

B)

Figure 12. (a) As in Figure 7 for the indicated experiment. (b) Perturbation kinetic energy averaged over the period April 1982–July 1984 derived from STACS PEGASUS data. (After Leaman *et al.*, 1987)

5. Stability of the STACS analyzed current

a. Development of initial conditions. To obtain an initial state more closely based on the observed current structure, we begin with the density data as a function of pressure and cross-stream dimension of Leaman *et al.* (1987). The data are interpolated to a grid with 10 m intervals in the vertical and 1.878 km in the horizontal, the same horizontal spacing as in the model. We linearly interpolate in the vertical to find the pressure at our constant density layer interfaces. The top layer has a density of 1023.6 kg m^{-3}, and for the successive nine layers, the density increases by .4 kg m^{-3} across each interface to a bottom layer value of 1027.2 kg m^{-3}. As will be seen in a moment, this concentrates vertical resolution at the base of the mixed layer and resolves the lower half of the cross-section with only three layers, but would appear to be an appropriate choice.

The layer-1 downstream motion field is drawn directly from the observed surface velocity data of Leaman *et al.* (1987). That for the remaining layers is specified then by integrating the thermal wind equation downward. This yields a motion field whose baroclinic structure, if not whose barotropic component, is in geostrophic balance with the mass field. As in the previous case, we integrate the model with downstream derivatives set to zero for several days during which the mass and flow fields may come into approximate balance with each other and with the lateral and bottom boundary conditions. For this integration and the subsequent stability tests, total mass flux through the channel is held constant at 31.7 × 10^6 m^3 s^{-1}. Finally, an averaging of the mass and downstream motion fields is performed over all time steps during the last few days of this integration. And, as with the idealized initialization, near the end of the integration, a cross-stream motion field to be used as the amplitude of the sinusoidal downstream perturbation is extracted.

The outcome of the above procedure is illustrated in Figure 13a, along with the extracted cross-stream motion field in Figure 13b. One of the primary differences between this and the two previous sets of initial conditions is a large increase in the PV in a horizontal band below the mixed layer. In addition, the potential vorticity increases monotonically from east to west along isopycnal surfaces, so that, in the interior, the necessary conditions for barotropic and baroclinic instability—at least according to QG theory—are not met. As in the previous case with topography, however, the lowest isopycnal interface merges with the channel bottom twice in the cross-section (Fig. 13). On the western side where $\delta_B > 1$, the flow is stabilized, but on the east side $\delta_B < 0$, so that instabilities are possible (Pedlosky, 1964). The X-Z structure of the cross-stream motion perturbation (Fig. 13b) is again complex, with values as high as 7.5 cm s^{-1} at 350 m depth.

b. Stability tests. The statistical summary of our experiments using initial conditions developed in the above fashion is given in Table 3. The information presented is in
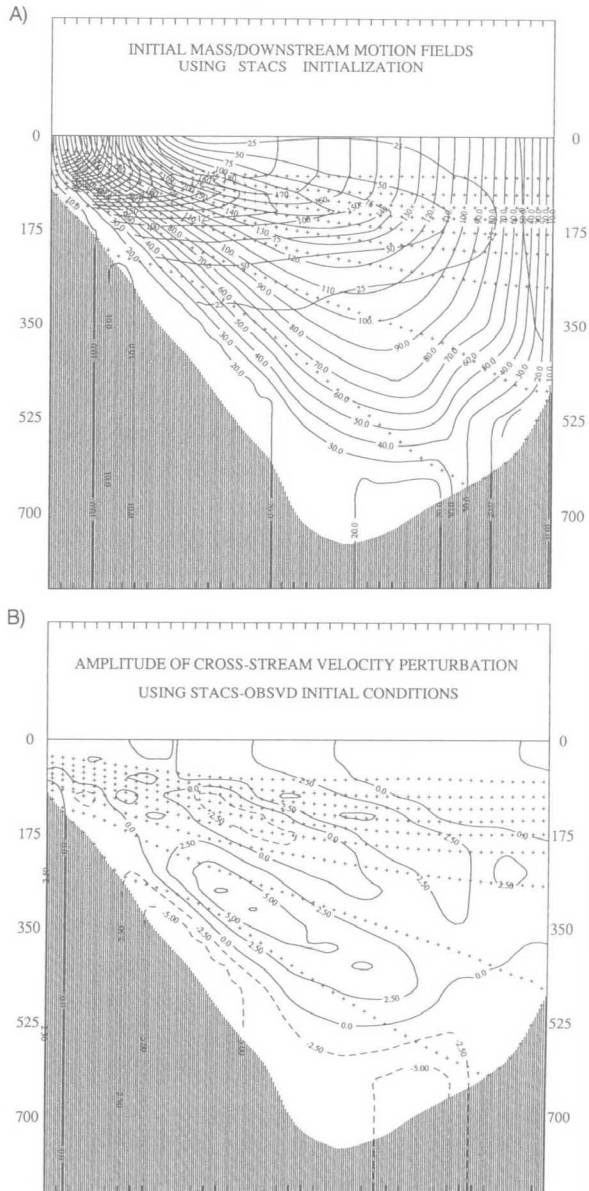
Figure 13. As in Figure 9 for the indicated experiment. Potential vorticity is contoured in (a) in units of 5×10^{-15} cm^{-2} s.

Table 3. As in Table 2 for experiments initialized from analysis of STACS observations.

λ (km)	60	90	120	150	180	210	240
$(K_e)_{max}$	.74	10.6	15.9	21.2	23.0	18.5	15.2
Time	7.1	14.2	20.0	34.2	37.1	30.0	40.8
$(K_e + P_e)_{max}$	1.1	13.5	21.4	27.5	32.2	25.9	21.5
Time	7.1	14.2	20.0	34.2	37.1	30.4	40.8
$(P \rightarrow K_e)_{max}$	.002	.085	.129	.086	.098	.06	.064
Time	1	13.0	19.2	21.7	15.2	28.3	15.8

many ways similar to that shown in Table 2 for the experiments using idealized initial data. A notable exception is in that the maximum values reached are 50 to 100% larger, though still less than half as large as those obtained with the flat bottom channel (Table 1). Once again, the short wavelength cutoff is between 60 and 90 km, and the maximum perturbation energy is reached for $\lambda = 180$ km, which has a period of ~4.5 days. Up to $\lambda = 180$ km, more time is required to reach the maximum energy levels. An interesting aspect of the $\lambda = 180$ km experiment is that the maximum baroclinic conversion rate is reached quite early because the half-wavelength harmonic (90 km), whose appearance is again derived from interaction with the bottom topography variation is amplifying then. A preliminary K_e maximum is therefore reached at ~15 days, representing amplification of both the 90 and 180 km perturbations, but primarily the former. Such an early $P \rightarrow K_e$ maximum is not obtained with $\lambda = 150$ km, suggesting that the half-wavelength harmonic (75 km) is near or below the short wavelength cutoff. The half-wavelength harmonics for $\lambda = 210$ and 240 km play an active role in the energy conversions up to approximately 30 days, after which the full wavelength perturbation becomes dominant. The figures given in the table are, thus, not fully applicable to those wavelengths, and these tests should not be considered conclusive in the cases with $\lambda > 180$ km. What this and the previous set of experiments with bottom topography point out is that perturbations in the wavelength range 90 to 120 km amplify more rapidly than longer ones—in fact, the maximum $P \rightarrow K_e$ here is reached for $\lambda = 120$ km—and thus would seem the most likely to first emerge from a field of random small perturbations. Furthermore, due to the possibility of interactions with the cross-stream bottom topographic variation (De Szoeke, 1975), the shorter wavelengths need not necessarily be present initially in order to emerge first as the dominant ones. These factors may be sensitive, however, to finite amplitude effects (Hart, 1981; Pedlosky, 1981) and to the limited length of the Straits of Florida. We will return to this issue in the final section.

The mean-eddy energetics for the $\lambda = 180$ km experiment (Fig. 14) are marked by two primary episodes of perturbation growth: the first centered at day 15 and dominated by growth in the 90 km wavelength (half-wavelength harmonic) and the second centered at day 35, dominated by growth in the initially specified 180 km wavelength. There is but one period, centered at ~7.5, days when the perturbation energy growth is apparently exponential. Again, the associated energy conversion is

A) MEAN AND PERTURBATION ENERGIES VS. TIME
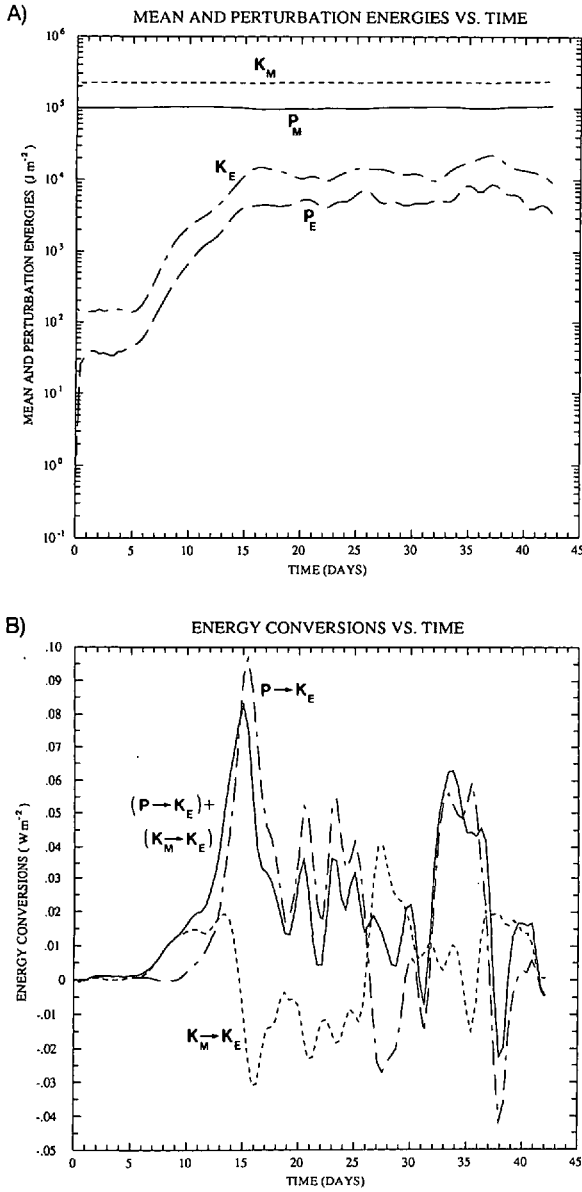
B) ENERGY CONVERSIONS VS. TIME

Figure 14. As in Figure 10 for the indicated experiment.

primarily $P \rightarrow K_e$. As in the previous case, barotropic conversion is the first to rise significantly above zero, this time near 7 days, but it then falls below zero as baroclinic conversion rises quickly to its first peak near day 15. Positive barotropic conversion apparently plays a role toward the end of this experiment, but the final peak in K_e is clearly associated with a corresponding peak in baroclinic conversion.

Of interest to note in Figure 14 is that potential and kinetic energy are being extracted from the mean flow efficiently enough so that P_m and K_m remain almost constant during the final two-thirds of the experiment, compared to the slow increase indicated in Figure 10a. The energetic behavior over the last several days of this experiment suggests that the pattern would perhaps continue indefinitely. It appears, then, that although the instability is marginal, barotropic and baroclinic (primarily the latter) conversion together provide an efficient mechanism for drawing surplus energy from the mean flow. We should also note that dissipation is of significance in the energy budget after Day 15 since the total energy conversion to K_e (solid curve) is generally somewhat above zero, and yet an equilibrium K_e level has apparently been reached (Fig. 14a). These perturbation energy curves may again be related to what may be expected for nonlinear release of baroclinic instability with a continual energy source and an intermediate level of friction (Pedlosky, 1987). The oscillations are far from identical in their physical makeup, but have the same essential character—the eddy energies grow and decay with corresponding changes in opposite directions of the mean potential energy (barely perceptible on the log scale of Fig. 14a).

The total and perturbation upper 60 m mean flow patterns at 37.1 days, near the maximum meander amplitude for the $\lambda = 180$ km experiment (Fig. 15), suggest that the meander has substantial amplitude in the western half of the channel and is perceptible over the entire channel.[5] The east-west dimension of the eddy inside the cyclonically curved portion of the meander is ~20 km, somewhat larger than that obtained with the previous set of initial conditions. Again, this is apparently larger than most meanders passing through 27N—at least as suggested from Johns and Schott's (1987) analysis of STACS current meter mooring data, but it is certainly within the range of meander amplitudes observed in the Straits (such as shown in Fig. 1).

The cross-section of perturbation kinetic energy for the 4-day period surrounding the final peak in K_e (Fig. 16) shows eddy energy concentrated on the cyclonically sheared side of the current core. Proceeding downward from the surface, this maximum shifts eastward and away from the bottom topography more rapidly than in the previous case, apparently because the current core does so (compare Figs. 9a and 13a). Also, because of the choice of isopycnal layer discretization, the lowest 2 layers occupy a much larger cross-sectional area than in the previous case; so that vertical resolution along the bottom topography on the west side of the channel is not as good.

This cross-section also emphasizes a feature suggested in the Leaman *et al.* (1987)

---

5. Leaman and Molinari's (1987) analysis of STACS PEGASUS data suggests that significant meander amplitudes do, in fact, extend across the Straits.
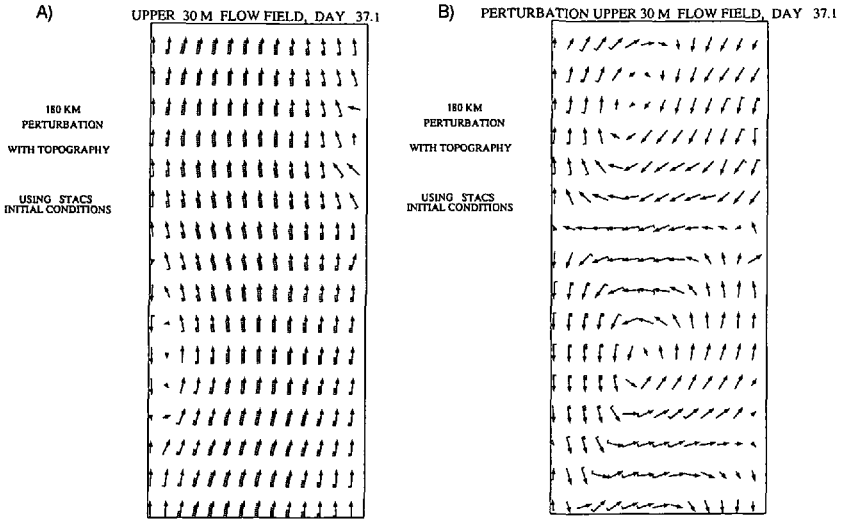
A)   UPPER 30 M FLOW FIELD, DAY 37.1   B)   PERTURBATION UPPER 30 M FLOW FIELD, DAY 37.1

180 KM
PERTURBATION
WITH TOPOGRAPHY

USING STACS
INITIAL CONDITIONS

180 KM
PERTURBATION
WITH TOPOGRAPHY

USING STACS
INITIAL CONDITIONS

Figure 15. As in Figure 11 for the $\lambda = 180$ km perturbation experiment with STACS analyzed initial data.

PERTURBATION KINETIC ENERGY
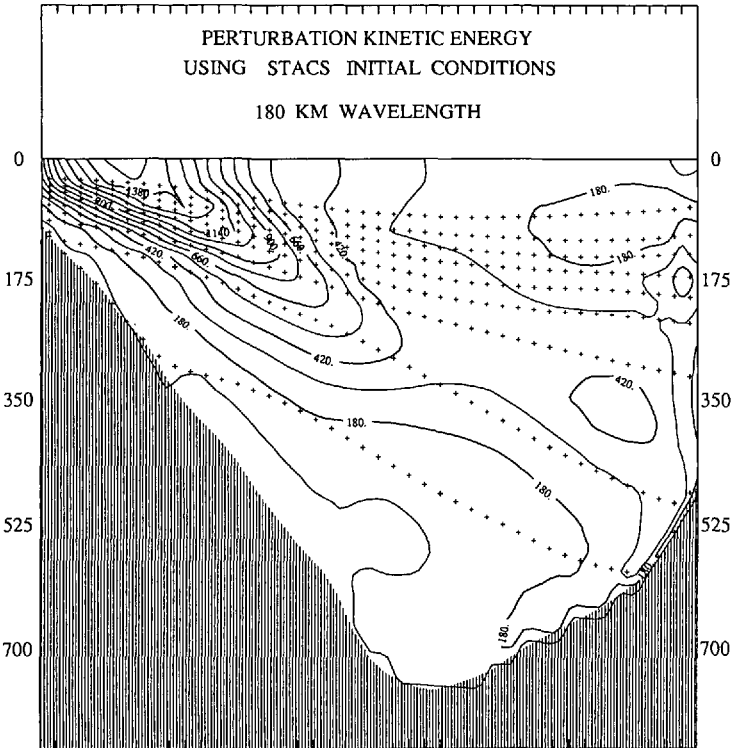USING STACS INITIAL CONDITIONS
180 KM WAVELENGTH

Figure 16. As in Figure 12a for the indicated experiment.

data (Fig. 12b) which was not as clearly produced using the idealized initial conditions (Fig. 12a): that is, a tongue of perturbation K_e extending down along the bottom topography on the eastern side of the channel. One possible mechanism for such a maximum is the existence of northward propagating bottom trapped waves (Rhines, 1970; Wang and Mooers, 1976), excited by the growing perturbation. The relative K_e minimum in the upper eastern portion of the cross-section suggests that these features are trapped below the strong stratification at the base of the mixed layer. The coherent existence of such waves in the Straits of Florida seems less likely than in our model because of the gaps in the eastern boundary (the Old Bahama and New Providence Channels) and its relatively short total length. However, the consistency of this model/data comparison suggests that bottom trapped waves may accompany meanders moving through the Straits. Moreover, the K_e maximum is likely also related to the existence of a necessary condition for baroclinic instability here where $\delta_B < 0$ (Pedlosky, 1964; De Szoeke, 1975).

6. Summary and conclusions

An isopycnic coordinate numerical model has been configured with ten layers in an infinitely long channel with the approximate width and bottom topography of the Straits of Florida at 27N in order to shed light on whether Florida Current meanders result from local dynamical instabilities. Two methods have been used to obtain a Florida Current-like mass/flow structure with which to initialize the model. The first is idealized but incorporates basic parameters from the STACS observational analyses. The second is based closely on the STACS mean hydrographic and PEGASUS current profiler data analyses of Leaman *et al.* (1987). The stability of the currents thus obtained to perturbations with a broad range of wavelengths has been ascertained by specifying initially a small amplitude perturbation in the cross-stream motion field, varying sinusoidally downstream, in individual wavelength experiments integrated out to as much as 45 days. In each series of experiments, the perturbation with $\lambda = 180$ km reaches the greatest amplitude. This is similar to the 170 km/5 days period meandering mode (the shortest of two dominant modes) which Johns and Schott (1987) extracted from STACS current meter mooring data.

As a point of reference, experiments in a flat bottom channel incorporating the same basic parameters from the STACS data were examined first. In this case, perturbations with $\lambda > 90$ km amplify considerably over a period of 20 to 25 days, and an energetics analysis has shown that the mechanism of growth is release of baroclinic instability. The $\lambda = 180$ km perturbation was described in some detail and found to achieve an amplitude much larger than meanders known to have been observed in the Straits. Also for this wavelength, during an approximately sixteen-day period of wave growth, the eddy kinetic energy (K_e) increases to substantially larger than the mean available potential energy (P_m) which has fallen to $\sim\frac{1}{3}$ of its original value. The mean structure of the initial current is thus greatly altered.

Meanders in approximately the same wavelength band amplify when the 27N bottom topography is incorporated, but the details of amplification and maximum amplitudes reached are quite different. The same perturbation wavelength, λ = 180 km, eventually exhibits greatest amplitude and K_e, but the latter is less than $\frac{1}{3}$ the value achieved in the flat bottom channel, and ~50% more time is required to achieve this maximum. In these experiments with bottom topography, the energetics suggest that baroclinic conversion $(P \rightarrow K_e)$ is the primary physical mechanism of meander growth, but the role of barotropic conversion $(K_m \rightarrow K_e)$ is not negligible. Another difference from the flat bottom case is in that the growth occurs during a series of events in which $P \rightarrow K_e$ rises rapidly for 3 to 4 days and then falls more slowly back to zero or a small negative value. The behavior seems similar to what one would expect for nonlinear release of baroclinic instability when friction is of intermediate importance (Pedlosky, 1987). The meanders thus produced have amplitude much more characteristic of those previously observed (e.g., see Schmitz and Richardson, 1968) and detected in the analysis of STACS moored current meter data by Johns and Schott (1987). The fact that K_m and P_m are only slightly affected during the meander growth suggests that the current is marginally unstable at best.

It was mentioned that in order for the initial perturbations to grow significantly, especially in the case with bottom topography, a crucial parameter of the idealized initialization scheme must be large enough: the surface cross-stream density variation. Through the thermal wind relation, this parameter strongly affects the baroclinicity of the mass/flow configuration. In the Leaman *et al.* (1987) analysis of STACS observations, the cross-stream surface density change is but 0.2 kg m^{-3} in the nearly homogeneous surface layer, which varies in depth from ~30 m on the west side to ~70 m on the east. The east-west density change increases rapidly with depth, however, to 1.4 kg m^{-3} at 70 m. When the corresponding parameter of the initialization is set to 0.3 kg m^{-3} or less, negligible amplification is obtained. The value used here, representing the actual change at 50 to 60 m depth, 1 kg m^{-3}, leads to generation of meanders having approximately the same scales as evident from the observations.

When the model is initialized with conditions developed from the Leaman *et al.* (1987) hydrographic and surface velocity data, a similar though higher amplitude behavior is obtained among the same scales of perturbations. The potential vorticity structure associated with this data set is dominated by a strong maximum surrounding the base of the surface mixed layer and extending upward to the surface west of the current core. A change in the sign of the isopycnal potential vorticity (IPV) gradient is present nowhere in the cross-section, however, and thus the commonly noted necessary conditions for barotropic and baroclinic instability are not met in the fluid interior. In the cases with idealized initial conditions, such a change in sign of the IPV gradient was present just west of the surface current core. In this case, however, a QG necessary condition for baroclinic instability is suggested in that the lowest isopycnal interface merges with the lower boundary on the east side where the ratio of their slopes, δ_B, is negative (De Szoeke, 1975; Pedlosky, 1964, 1987). The experimental results suggest

that the structure is again weakly unstable, and the major portion of meander growth is associated with baroclinic energy conversion, indicating that the primary mechanism is release of baroclinic instability. Barotropic conversion is the first to rise significantly above zero, however, and might be considered the initiator of meander growth in both sets of experiments with bottom topography.

In order to keep the model relatively simple and to make optimal use of the STACS data anlyses at 27N, two important issues have been ignored here: (1) the effects of downstream variations in channel geometry and (2) the actual time which meanders spend in the Straits. The first of these likely exerts both stabilizing and destabilizing influences depending on position within the channel. In addition, the south-southeast to north-northwest tilt of the eastern boundary at 27N and to the south results in a significant mean westward component of motion at middle depths up to 30 km from that boundary (see, e.g., Leaman and Molinari, 1987). By necessity, this mean cross-stream motion is absent from our initial conditions. While experiments using bottom topography cross-sections appropriate for other positions within the Straits may help give a first-order estimate as to the effects of irregularities such as the Miami Terrace, a more complex and computationally expensive model will be required to sort out all the effects of the downstream variations in channel geometry.

Our results may be qualified with respect to the actual length of the Straits by considering the rate at which meanders move downstream in the model, as well as that suggested in the data analysis of Johns and Schott (1987). Both model and observation indicate a propagation speed of $\sim$40 cm s^{-1}. Thus, a meander well spend approximately eight days traveling from 25N, where the Current is completing the turn from eastward to northward, to 27.5N at the north end of the Bahama Bank. Our time series energetics would suggest that this is not enough time for a small, perhaps poorly organized perturbation to grow into a substantial meander. However, if the wave growth occurs in spurts, such as in our experiments with bottom topography, a perturbation which is reasonably well organized as it enters this segment of the Straits might well grow to amplitudes suggested in Figure 1 before exiting to the north.

The experiments described here suggest that perturbations with downstream scales somewhat greater than the short wavelength cutoff, but still considerably less than 180 km (for which the highest amplitudes have been achieved here in each case), become organized to begin drawing energy from the mean flow more quickly than the longer wavelength perturbations. Three additional experiments were run to gain insight into meander development in a competitive environment, corresponding to the three sets of experiments summarized in Tables 1, 2, and 3. Here, the channel length was 960 km, the along-channel grid spacing 7.5 km, and the downstream perturbation structure was developed using a random number generator. In each case, a relatively short wavelength was the first to emerge with significant amplitude, although more time was required in general for such amplitude to be reached than in the individual wavelength experiments. Spectral decomposition of the barotropic streamfunction

showed that, in the flat bottom experiment, $\lambda = 137$ km emerged by day 22, but by day 37 had yielded to $\lambda = 160$ km, which was dominant for the remainder of the 45 day experiment. Using idealized initial conditions and bottom topography, even smaller wavelengths appeared first. $\lambda = 87$ km became dominant by day 22 and yielded to $\lambda = 106$ and 137 km by 40 days. Correspondingly, with initial conditions developed from the STACS data, $\lambda = 96$ km became the first dominant wavelength by 22 days, but yielded to $\lambda = 192$ km for the remainder of the 41-day experiment. An important effect brought out by these, as well as the individual λ, experiments is the slight destabilization of the current with respect to wavelengths closer to the short wavelength cutoff when bottom topography is present, previously demonstrated for a two-layer model by Blumsack and Gierasch (1972) and Mechoso (1980) when $\delta_B < 0$.

An interesting question is whether, in this environment including all wavelengths, emergence of the longer waves is due primarily to their amplification from the mean flow or to a nonlinear transfer of energy from the shorter waves, which draw energy from the mean flow earlier and are weakening. The results from the individual λ experiments would suggest that the longer waves would, in fact, begin drawing energy efficiently from the mean flow several days after the shorter ones. Examination of the energy conversion diagrams (not shown) for the arbitrary perturbation experiments does not suggest, however, that this is necessarily the case. Some relevance of the preliminary work on finite amplitude instability by Hart (1981) and Pedlosky (1981) may be suggested. They find that, in some cases, the wave which will be observed is not the one with maximum growth rate (i.e., here, the shorter waves) but rather with the capacity for the largest amplitude (longer waves). According to Johns and Schott (1987), the shortest dominant meander mode at 27N has $\lambda = 170$ km. Our nonlinear model results, both individual λ and arbitrary perturbation, suggest that shorter wavelengths ($85 < \lambda < 120$ km) may be more linearly unstable in the Straits, but those in the 140–190 km range are more likely to dominate. In actuality, this competition for mean flow energy and transfer among wavelengths may not be relevant in the Straits of Florida, where a perturbation likely must already be well organized as it enters in order to amplify significantly before exiting. Further investigation of this question must await future work.

Finally, De Szoeke (1975) considered modification to classical linear theory of baroclinic instability (Eady, 1949) due to interaction with cross-stream bottom topographic variation such as exists in the Straits of Florida. He derived two classes of instabilities, termed *modified Eady* and *hybrid* instabilities. The former modification is characterized as not being fundamental in that the primacy of the baroclinic energy source is maintained. Regarding the latter, however, topographic drag forces are found to redistribute energy among the baroclinic energy source ($P \rightarrow K_e$) and the rate at which fluctuation Reynolds stresses work on the mean horizontal shear ($K_m \rightarrow K_e$). In addition, the growth of *hybrid* fluctuations is a relatively small demand on the energy source. In our experiments with the Straits bottom topography, barotropic energy

conversion is non-negligible and meander growth is only a minor drain on the mean available potential energy. Thus, De Szoeke's *hybrid* baroclinic instability (or a variation of it) is suggested as a possible mechanism for the model meander growth. This sort of topographic interaction is particularly suggested by the appearance of higher harmonics (especially the one which is half the length of the single perturbation wavelength initially specified) if the current is unstable to the harmonic. On the other hand, when he performs dimensional calculations of wavelength, period, and e-folding time scale of the most rapidly growing waves, using parameters appropriate to the Straits of Florida, the hybrid instabilities involve either a much slower growth rate or longer wavelengths than obtained here. Only a type of *modified Eady* instability (ME1) appears to have all characteristics in common with some of the meanders generated in the current model: wavelengths of 110 to 130 km, periods of 2.6 to 3 days and e-folding time scales of 6.6 to 9.8 days. Further agreement with De Szoeke's (1975) findings would likely be revealed by a more in-depth comparison, but such is beyond the scope of the current paper.

REFERENCES

Bleck, R. 1984. An isentropic coordinate model suitable for lee cyclogenesis simulation. Riv. Meteorol. Aeronaut., *44*, 189–194.
—— 1985. On the conversion between mean and eddy components of potential and kinetic energy in isentropic and isopycnic coordinates. Dyn. Atmos. Oceans, *9*, 17–37.
Bleck, R. and D. Boudra. 1986. Wind-driven spin-up in eddy-resolving ocean models formulated in isopycnic and isobaric coordinates. J. Geosphys. Res., *91(C6)*, 7611–7621.
Bleck, R., R. Ontken and J. D. Woods. 1988. A two-dimensional model of mesocale frontogenesis in the ocean. Quart. J. Royal Met. Soc., *114*, 347–371.
Blumsack, S. and P. J. Gierasch. 1972. Mars: the effects of topography on baroclinic instability. J. Atmos. Sci., *35*, 1314–1318.
Boris, J. P. and D. L. Book. 1973. Flux-corrected transport. I. SHASTA. A fluid transport algorithm that works. J. Computat. Phys., *11*, 38–69.
Brooks, I. H. and P. P. Niiler. 1977. Energetics of the Florida Current. J. Mar. Res., *35*, 163–191.
Charney, J. G. and M. E. Stern. 1962. On the stability of internal baroclinic jets in a rotating atmosphere. J. Atmos. Sci., *19*, 159–172.
De Szoeke, R. A. 1975. Some effects of bottom topography on baroclinic stability. J. Mar. Res., *33*, 93–122.
Duing, W. O. 1975. Synoptic studies of transients in the Florida Current. J. Mar. Res., *33*, 53–73.
Eady, E. T. 1949. Long waves and cyclone waves. Tellus, *1*, 33–52.
Hart, J. E. 1981. Wave number selection in nonlinear baroclinic instability. J. Atmos. Sci., *38*, 400–408.

Hoskins, B. J. and F. P. Bretherton. 1972. Atmospheric frontogenesis models, mathematical formulation and solution. J. Atmos. Sci., *29*, 11–37.

Johns, W. E. 1988. One-dimensional baroclinically unstable waves on the Gulf Stream potential vorticity gradient near Cape Hatteras. Dyn. Atmos. Oceans, *11*, 323–350.

Johns, W. E. and F. Schott. 1987. Meandering and transport variations of the Florida Current. J. Phys. Oceanogr., *17*, 1128–1147.

Larsen, J. C. and T. B. Sanford. 1985. Florida Current volume transports from voltage measurements. Science, *227*, 302–303.

Leaman, K. D., and R. L. Molinari. 1987. Topographic modification of the Florida Current by Little Bahama and Great Bahama Banks. J. Phys. Oceanogr., *17*, 1724–1736.

Leaman, K. D., R. L. Molinari, and P. Vertes. 1987. Structure and variability of the Florida Current at 27°N, April 1982–July 1984. J. Phys. Oceanogr., *17*, 565–583.

Lee, T. N. and D. A. Mayer. 1977. Low-frequency current variability and spin-off eddies along the shelf off southeast Florida. J. Mar. Res., *35*, 193–220.

Lee, T. N., F. Schott and R. Zantopp. 1985. Florida Current, low-frequency variability as observed with moored current meter stations during April 1982–June 1983. Science, *227*, 298–301.

Lee, T. N. and N. P. Smith, G. Maul, A. D. Kirwan, F. Schott, K. D. Leaman and J. R. Proni. 1986. Physical oceanographic study of Florida's Atlantic Coast Transport Study (FACTS) Final report. Vol 2—Technical rept, University of Miami, 386 pp.

Lee, T. N. and E. Williams. 1988. Wind-forced transport fluctuations of the Florida Current. J. Phys. Oceanogr., *18*, 937–946.

Mechoso, C. 1980. Baroclinic instability of flows along sloping boundaries. J. Atmos. Sci., *37*, 1393–1399.

Molinari, R. L., W. D. Wilson and K. Leaman. 1985. Volume and heat transports of the Florida Current. Science, *227*, 295–297.

Niiler, P. P. and W. S. Richardson. 1973. Seasonal variability of the Florida Current. J. Mar. Res., *31*, 144–167.

Orlanski, I. and M. D. Cox. 1973. Baroclinic stability in ocean currents. Geophys. Fluid Dyn., *4*, 297–332.

Pedlosky, Joseph. 1964. The stability of currents in the atmosphere and ocean: Part I. J. Atmos. Sci., *21*, 201–219.

—— 1981. The nonlinear dynamics of baroclinic wave ensembles. J. Fluid. Mech., *102*, 169–209.

—— 1987. Geophysical Fluid Dynamics. 2nd Edition. Springer-Verlag. New York. 710 pp.

Rhines, P. 1970. Edge-, bottom- and Rossby waves in a rotating stratified fluid. Geophys. Fluid Dyn., *1*, 273–302.

Schmitz, W. J., Jr. and W. S. Richardson. 1968. On the transport of the Florida Current. Deep-Sea Res., *15*, 679–693.

Schott, F., T. N. Lee and R. Zantopp. 1988. Variability of structure and transport of the Florida Current in the period range of days to seasonal. J. Phys. Oceanogr., *18*, 1209–1230.

Wang, D.-P. and C. N. K. Mooers. 1976. Coastal-trapped waves in a continuously stratified ocean. J. Phys. Oceanogr., *6*, 853–863.

Zalesak, S. T. 1979. Fully multi-dimensional flux-corrected transport algorithm for fluids. J. Computat. Phys., *31*, 335–362.

Zantopp, R., K. D. Leaman and T. N. Lee. 1987. Florida Current Meanders: A close look in June–July, 1984. J. Phys. Oceanogr., *17*, 584–595.